REGULAR PAPER

Accurate Estimation of Carotid Luminal Surface Roughness Using Ultrasonic Radio-Frequency Echo

Kosuke Kitamura, Hideyuki Hasegawa, and Hiroshi Kanai

REGULAR PAPER

Accurate Estimation of Carotid Luminal Surface Roughness Using Ultrasonic Radio-Frequency Echo

Kosuke Kitamura[1], Hideyuki Hasegawa[1,2], and Hiroshi Kanai[1,2*]

[1]*Graduate School of Biomedical Engineering, Tohoku University, Sendai 980-8579, Japan*
[2]*Graduate School of Engineering, Tohoku University, Sendai 980-8579, Japan*

It would be useful to measure the minute surface roughness of the carotid arterial wall to detect the early stage of atherosclerosis. In conventional ultrasonography, the axial resolution of a B-mode image depends on the ultrasonic wavelength of $150\,\mu\text{m}$ at $10\,\text{MHz}$ because a B-mode image is constructed using the amplitude of the radio-frequency (RF) echo. Therefore, the surface roughness caused by atherosclerosis in an early stage cannot be measured using a conventional B-mode image obtained by ultrasonography because the roughness is 10–$20\,\mu\text{m}$. We have realized accurate transcutaneous estimation of such a minute surface profile using the lateral motion of the carotid arterial wall, which is estimated by block matching of received ultrasonic signals. However, the width of the region where the surface profile is estimated depends on the magnitude of the lateral displacement of the carotid arterial wall (i.e., if the lateral displacement of the arterial wall is $1\,\text{mm}$, the surface profile is estimated in a region of $1\,\text{mm}$ in width). In this study, the width was increased by combining surface profiles estimated using several ultrasonic beams. In the present study, we first measured a fine wire, whose diameter was $13\,\mu\text{m}$, using ultrasonic equipment to obtain an ultrasonic beam profile for determination of the optimal kernel size for block matching based on the correlation between RF echoes. Second, we estimated the lateral displacement and surface profile of a phantom, which had a saw tooth profile on its surface, and compared the surface profile measured by ultrasound with that measured by a laser profilometer. Finally, we estimated the lateral displacement and surface roughness of the carotid arterial wall of three healthy subjects (24-, 23-, and 23-year-old males) using the proposed method. © 2012 The Japan Society of Applied Physics

1. Introduction

Medical ultrasound is clinically used to make a diagnosis for various organs, and because it is noninvasive and relatively stress free for patients, it can be repeatedly employed to confirm time-dependent changes. Ultrasound B-mode imaging is widely used for the morphological diagnosis of the arterial wall, particularly for measurement of the intima–media thickness.[1–3] In addition, methods for evaluating the viscoelasticity of the arterial wall have recently been developed[4–9] because the mechanical properties of the arterial wall are related to atherosclerotic changes.

Diagnosis of atherosclerosis in an early stage is important to prevent the occurrence of strokes and heart attacks. In the early stage of atherosclerosis, the luminal surface of an arterial wall becomes rough as a result of endothelial damage.[10,11] It would be useful to measure such minute surface roughness of the carotid arterial wall for early diagnosis of atherosclerosis. For this purpose, sub-micron resolution is required because endothelial cells are 10–$20\,\mu\text{m}$ thick.[12] In conventional ultrasonography, the axial resolution of a B-mode image depends on the ultrasonic wavelength of $150\,\mu\text{m}$ at $10\,\text{MHz}$ because a B-mode image is constructed using the amplitude of the RF echo. Therefore, the surface roughness caused by atherosclerosis in an early stage cannot be measured by conventional B-mode imaging using ultrasonography.

Wilhjelm *et al.* and Kudo *et al.* evaluated micron-order surface roughness.[13–15] They focused on the angle-dependent characteristics of echo energy or echo amplitude and frequency characteristics.[16] However, their methods cannot measure the surface profiles of objects. Arihara *et al.* measured the micron-order surface profile of an object made of silicone rubber using the phase shift of RF echoes during the sweeping of an ultrasonic beam.[17] However, a minute surface profile cannot be measured *in vivo* using this method because the carotid arterial wall moves in the radial (= axial) direction but also in the longitudinal (= lateral) direction.[18] Thus, it is difficult to distinguish the lateral motion due to the probe sweeping and the arterial longitudinal motion.

Cinthio *et al.* suggested minute roughness measurement by combining phased-tracking and block matching.[19–22] They estimated the surface profiles of silicone phantoms, which had ten saw tooth shapes on their surfaces, during their lateral motion without sweeping an ultrasonic beam. During a cardiac cycle, the carotid arterial wall moves not only in the radial direction but also in the longitudinal direction. This longitudinal movement induces the axial displacement (change in height during longitudinal movement) of the surface at an ultrasonic beam when the surface is rough. They could measure this axial displacement during the lateral movement of the phantoms of $6\,\text{mm}$ using the phased-tracking method,[21–23] which can measure the axial displacement with a sub-micron resolution and is used in various applications, such as the measurement of hearts[24–26] and arteries.[7,9] However, the longitudinal displacement of the carotid artery is less than $1\,\text{mm}$, and this would limit the length of the region of measurement. In this paper, we propose a method to increase the measured region using several ultrasonic beams.

2. Principles

2.1 Accurate estimation of surface roughness of arterial wall

In this study, the axial (z-axis) displacement caused by surface roughness is measured at an ultrasonic beam position. During cardiac systole, the vascular diameter is dilated in the radial direction (z-axis) and the vascular wall is also moved in the longitudinal direction (x-axis)[18] owing to the force caused by the arch of the aorta being pulled by the contraction of the heart in cardiac systole.

Figure 1 illustrates displacements caused by a heart beat. The lateral position of the m-th ultrasonic beam is denoted by x_m ($x_m = m \cdot \delta x$, where δx is the lateral spacing of the sampled points). Let us define the frame interval ΔT. The

*E-mail address: kanai@ecei.tohoku.ac.jp
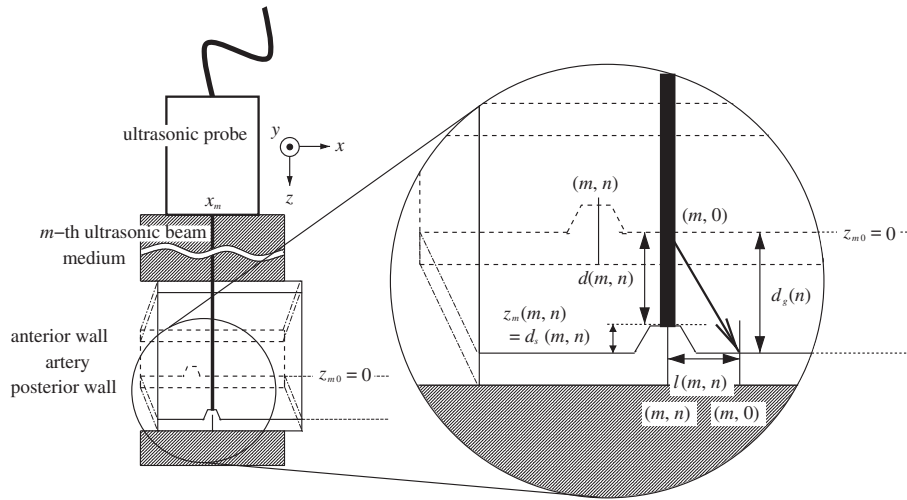
© 2012 The Japan Society of Applied Physics

Fig. 1. Illustration of displacements between 0-th frame and n-th frame.

axial (z-axis) displacement of the posterior wall surface $\Delta d(x_m, n) \equiv \Delta d(m, n)$ between the n-th frame [t (s)] and the $(n+1)$-th frame [$(t + \Delta T)$ (s)] is obtained from the difference between the axial position $z(x_m, n) \equiv z(m, n)$ of the surface in the n-th frame and the axial position $z(x_m, n+1) \equiv z(m, n+1)$ in the $(n+1)$-th frame as follows:

$$\Delta d(m, n) = z(m, n+1) - z(m, n). \tag{1}$$

Using the phase shift $\Delta\theta(m, n)$ of RF signals between the n-th frame and the $(n+1)$-th frame, which is caused by expansion of the artery and surface roughness, the axial displacement $\Delta d(m, n)$ at the position x_m of an ultrasonic beam is estimated as follows:[21,22]

$$\Delta\hat{d}(m, n) = \frac{c}{2\omega_0} \Delta\hat{\theta}(m, n), \tag{2}$$

where c is the sound speed in the medium (1540 m/s) and ω_0 ($= 2\pi f_0$) is the center angular frequency of ultrasound (center frequency $f_0 = 10$ MHz). The axial displacement $\hat{d}(m, n)$ between the 0-th frame and the n-th frame is calculated by accumulating instantaneous displacements $\{\Delta\hat{d}(m, n)\}$ estimated by the phased-tracking method[21,22] as follows:

$$\hat{d}(m, n) = \sum_{n=0}^{n} \Delta\hat{d}(m, n). \tag{3}$$

As shown in Fig. 2(a), which shows a B-mode image of the carotid artery in the short-axis view, RF signals from the luminal surface of the carotid artery are obtained in a very limited region of 0.8 mm in the transverse direction. Thus, the position of the ultrasonic probe can be kept within ±0.4 mm in the transverse direction by keeping the echoes from the luminal surface from being visualized. Also, Fig. 2(b) is a B-mode image of a carotid artery in the long-axis view. If the lateral position of the ultrasonic probe changes by a few millimeters, the lateral displacement caused by the lateral motion of the ultrasonic probe can be estimated using block matching. However, the change in the lateral position of the ultrasonic probe may introduce a change in sound speed in the medium between the skin and the artery. When the lateral velocity of the ultrasonic probe is 0.5 mm/s, the change in the lateral position of the
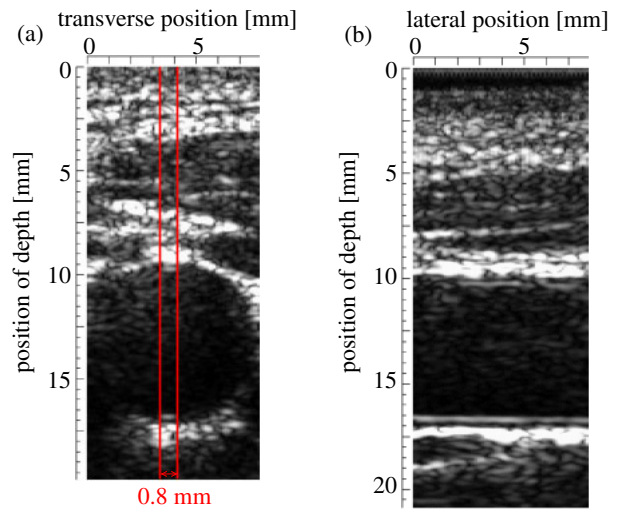

Fig. 2. (Color online) B-mode image of carotid artery (24-year-old healthy male). (a) Short axis view. Red lines show the region where RF signals from the luminal surface of the carotid arterial wall could be obtained. (b) Long axis view.

ultrasonic probe between frames is 0.003 mm, when the frame rate is 160 Hz. The lateral displacement between frames should be considered because the axial displacement between frames is estimated in the phased-tracking method, as shown in eq. (2). The transmitting region of ultrasound shifts by about $0.003/3 \times 100\% = 0.1\%$ because the aperture size was 3 mm. The difference in sound speed is $5.8\% \times 0.001 = 0.0058\%$ because the variation of sound speed *in vivo* is about 5.8% (soft tissue: 1540 m/s–fat: 1450 m/s[27]). Therefore, the effect of the change in sound speed on the estimation of the distance of 15 mm from the skin surface to the artery is 0.87 µm and it can be neglected because it is much smaller than the surface roughness (10 µm), which is desired to be measured.

As shown in Fig. 1, the estimated displacement $\hat{d}(m, n)$ is composed of the global displacement of the arterial wall $d_g(n)$ due to the expansion of the artery and the displacement $d_s(m, n)$ caused by the surface profile (roughness) as follows:[19]

$$\hat{d}(m,n) = d_{\mathrm{g}}(n) + d_{\mathrm{s}}(m,n). \qquad (4)$$

In a region of a few millimeters in the x-direction, the instantaneous axial displacements $\{\Delta d_{\mathrm{g}}(m+i,n)\}$ ($i = 0,1,2,\ldots,M-1$) caused by global wall motion between the n-th frame and the $(n+1)$-th frame at positions $\{x_{m+i}\}$ are assumed to be the same because the wavelength of the pulse wave is a few meters and the pulse repetition frequency is 13 kHz. Therefore, the instantaneous axial displacement $\Delta d_{\mathrm{g}}(n)$ caused by global wall motion can be estimated by averaging the axial instantaneous displacements $\{\Delta d(m,n)\}$, as follows:

$$\hat{d}_{\mathrm{g}}(n) = \sum_{n=0}^{n} \Delta \hat{d}_{\mathrm{g}}(n), \qquad (5)$$

$$\Delta \hat{d}_{\mathrm{g}}(n) = \frac{1}{M} \sum_{m=0}^{M-1} \Delta \hat{d}(m,n), \qquad (6)$$

where M is the number of ultrasonic beams, $d(m,n)$ is the axial displacement at the position x_m of an ultrasonic beam, and $\hat{d}_{\mathrm{g}}(n)$ is the axial displacement caused by global wall motion between the 0-th frame and the n-th frame.

Finally, the surface profile $z_m(x; z_{m0})$ estimated at the m-th ultrasonic beam is expressed as follows:[19]

$$\hat{z}_m(x; z_{m0}) \equiv \hat{z}_m[x_m + \hat{l}(m,n); z_{m0}] \qquad (7)$$

$$= z_{m0} + \sum_{n=0}^{n} \Delta \hat{d}_{\mathrm{s}}(m,n), \qquad (8)$$

$$\Delta \hat{d}_{\mathrm{s}}(m,n) = \Delta \hat{d}(m,n) - \Delta \hat{d}_{\mathrm{g}}(n), \qquad (9)$$

where z_{m0} is the initial height, which is determined as described in §2.3.

Then, the arterial longitudinal displacement $l(m,n)$ should be estimated to obtain the surface profile $z_m(x; z_{m0})$ as a function of lateral position $x_m + l(m,n)$. Using the block matching,[28,29] the estimated lateral displacement $l(m,n)$ of the arterial wall at the m-th ultrasonic beam between the 0-th frame and the n-th frame is given by[19]

$$\hat{l}(m,n) = \sum_{n=0}^{n} \Delta \hat{l}(m,n), \qquad (10)$$

where $\Delta \hat{l}(m,n)$ is the estimated instantaneous lateral displacement of the arterial wall between frames. The instantaneous lateral displacement $\Delta l(m,n)$ is estimated as described in §2.2. Using the estimated lateral displacement $\hat{l}(m,n)$, the lateral position of a point on the arterial wall where the m-th ultrasonic beam crosses at the n-th frame is defined as $(x_m, n) \equiv (m,n) = [x_m + \hat{l}(m,n)]$.

2.2 Estimation of longitudinal displacement of arterial wall based on block matching using correlation function

In the present study, the lateral displacement $l(m,n)$ is estimated by block matching[28,29] between RF echoes. To apply block matching, the size of the correlation kernel, which is defined by the size of $(2a+1)$ [lateral] $\times (2b+1)$ [axial] (sampled points), was examined. An RF echo at position (x,z) in the n-th frame and the central position of the correlation kernel are defined as $s_n(x,z)$ and (x_m, z_{m0}), respectively. The initial lateral position x_m is manually assigned in the first frame and the initial axial position z_{m0} is automatically assigned at a point shallower than the point at the maximum value of the envelope of the RF signal by β points (β: constant value) and its position is tracked in the successive frames by block matching. The normalized correlation function $C_n[\Delta l(m,n), \Delta d_{\mathrm{sp}}(m,n)]$ at the lateral lag $\Delta l(m,n)$ and axial lag $\Delta d_{\mathrm{sp}}(m,n)$ is calculated from RF signals $s_n(x,z)$ and $s_{n+1}(x,z)$ in the n-th frame and $(n+1)$-th frame as follows:

$$C_n[\Delta l(m,n), \Delta d_{\mathrm{sp}}(m,n)] = \frac{\displaystyle\sum_{i=-a}^{a} \sum_{j=-b}^{b} S_n(i,j) S_{n+1}\left[i + \frac{\Delta l(m,n)}{\delta x}, j + \frac{\Delta d_{\mathrm{sp}}(m,n)}{\delta z}\right]}{\sqrt{\displaystyle\sum_{i=-a}^{a}\sum_{j=-b}^{b} S_n^2(i,j)} \sqrt{\displaystyle\sum_{i=-a}^{a}\sum_{j=-b}^{b} S_{n+1}^2\left[i + \frac{\Delta l(m,n)}{\delta x}, j + \frac{\Delta d_{\mathrm{sp}}(m,n)}{\delta z}\right]}}, \qquad (11)$$

$$S_n(i,j) = s_n(x_m + i \cdot \delta x, z_{m0} + j \cdot \delta z) - \bar{s}_n, \qquad (12)$$

where δx and δz are the lateral and axial spacings of sampled RF echo, respectively, and $\bar{s}_n$ is the spatial mean of RF signals in a kernel in the n-th frame. The instantaneous lateral and axial displacements $\Delta l(m,n)$ and $\Delta d_{\mathrm{sp}}(m,n)$ of the arterial wall are determined from the lags $\Delta \hat{l}(m,n)$ and $\Delta \hat{d}_{\mathrm{sp}}(m,n)$, respectively, which maximize the normalized correlation function $C_n[\Delta l(m,n), \Delta d_{\mathrm{sp}}(m,n)]$. In the estimation of the lateral displacement, the lateral spatial resolution δx depends on the ultrasonic beam interval (100 μm). If the frame rate is 160 Hz, the lateral displacement is 9 μm between frames when the average lateral moving speed of the carotid arterial wall is 1.4 mm/s (measured in the carotid artery of a healthy subject). Thus, the lateral spatial resolution δx, which depends on the interval of ultrasonic beams (100 μm), is not sufficient because the lateral displacement between frames is smaller than the lateral spatial resolution δx. To solve this problem, the normalized correlation function $C_n[\Delta l(m,n), \Delta d_{\mathrm{sp}}(m,n)]$ was interpo- lated using reconstructive interpolation.[30,31] Figure 3 shows the estimated lateral displacements $\{\hat{l}(m,n)\}$ after interpola- tion with various interpolation factors. As shown in Fig. 3, 100 point interpolation is sufficient to estimate the lateral displacement between frames of 9 μm, which is a typical arterial longitudinal displacement. Therefore, in this study, the lateral spatial resolution after interpolation $\delta x'$ was set at $\delta x/100$. Similarly, the axial spatial resolution after inter- polation $\delta z'$ was set at $\delta z/100$, where δz is the original spacing of the sampled points in the z-direction. The estimated axial displacement $\Delta d_{\mathrm{sp}}(m,n)$ also corresponds to global wall motion between the n-th frame and the $(n+1)$-th frame. However, the displacement caused by global wall motion was already estimated as the axial displacement $\hat{d}_{\mathrm{g}}(n)$ by the phased-tracking method. In this study, the axial displacement $\hat{d}_{\mathrm{g}}(n)$ was adopted as the displacement caused by global wall motion because an excellent accuracy in the estimation of the axial displace-
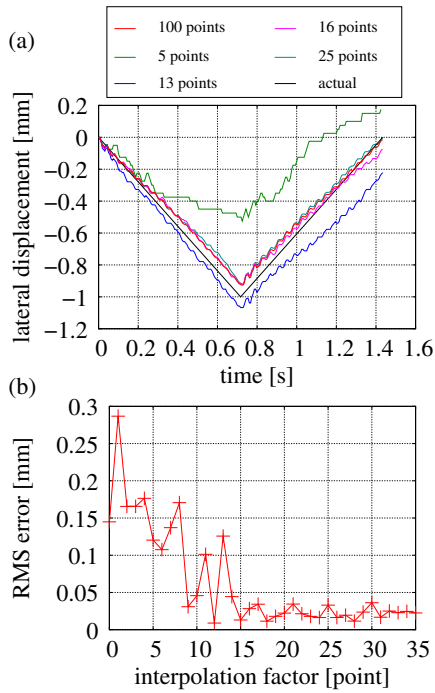
Fig. 3. (Color online) (a) Estimated lateral displacements $\{l(m,n)\}$, which were interpolated using various numbers of points, and actual displacement $l_a(m,n)$ (black line). (b) Distribution of RMS errors for different interpolation factors.
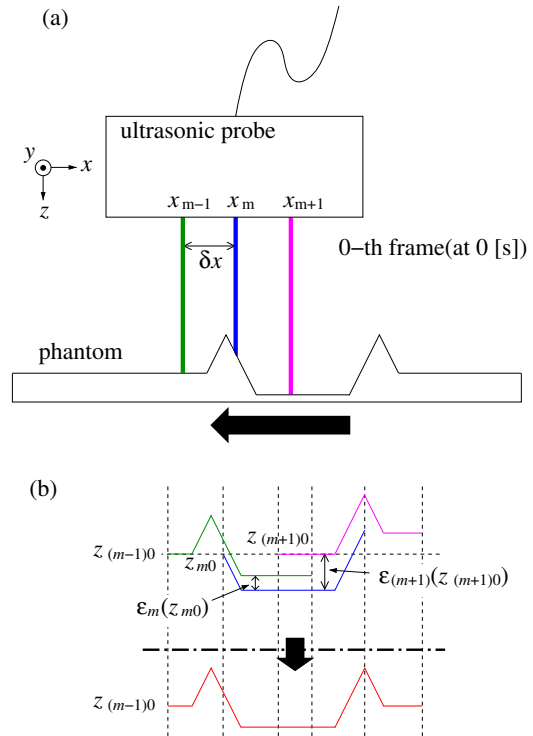

Fig. 4. (Color online) Illustration of expansion of region to estimate surface profile. (a) Data acquisition. (b) Estimated surface profiles before expansion (green, blue, and pink lines) and after expansion (red line).

Fig. 5. (Color online) Accurate estimation of carotid lumial surface roughness proposed in this study.

ment has already been achieved by the phased-tracking method.

2.3 Expansion of region of accurate estimation of surface roughness

Thus far, we considered the estimation of the surface profile using an ultrasonic beam. However, the longitudinal displacement of the carotid artery is less than 1 mm, and this would limit the length of the region of measurement. Therefore, we proposed a method to increase the length of the measured region using several ultrasonic beams. The minute surface profile $z_m(x; z_{m0})$ in eq. (8) is estimated with respect to each beam (m-th beam). If the lateral displacement of the arterial wall is 1 mm and the beam intervals are 0.1 mm, regions of 0.9 mm overlap (i.e., 9 beams overlap). Thus, we connect the surface profiles estimated using adjacent ultrasonic beams by adjusting the initial height z_{m0} to expand the region for the accurate estimation of surface roughness. For this purpose, the RMS difference $\epsilon_m(z_{m0})$ between surface profiles obtained at the $(m-1)$-th and m-th beams in the overlapping region is evaluated as follows [Figs. 4(a) and 4(b)]:

$$\epsilon_m(\hat{z}_{m0}) = \sqrt{\frac{1}{N}\sum_{n=0}^{N-1}[\hat{z}_m(x;\hat{z}_{m0}) - \hat{z}_{(m-1)}(x;\hat{z}_{(m-1)0})]^2}, \quad (13)$$

where z_{00} is assumed to be zero. The optimal initial height $\hat{z}_{m0}$ is determined by minimizing $\epsilon_m(\hat{z}_{m0})$. The surface profile $z(x)$ in the overlapping region is estimated as follows:

$$\hat{z}(x) = \frac{1}{M_{\text{overlap}}(x)}\sum_{m=0}^{M_{\text{total}}}\hat{z}_m(x;\hat{z}_{m0}), \quad (14)$$

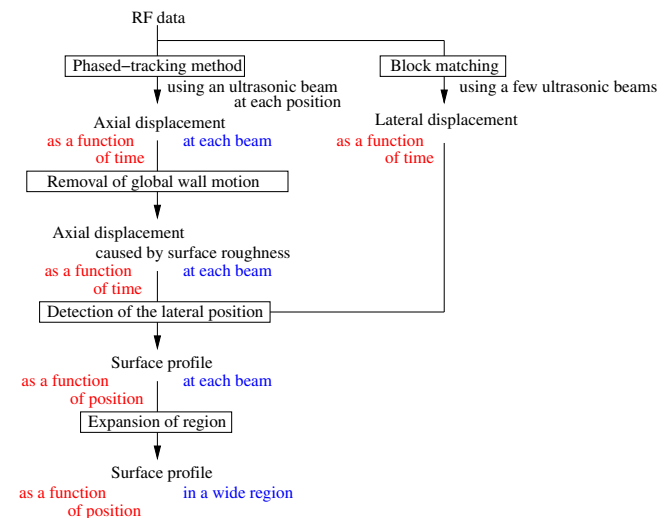where M_{total} means the total number of ultrasonic beams and

$M_{\text{overlap}}(x)$ is the number of surface profiles, which are estimated at the lateral position x. If the surface profiles are not estimated at x, the surface profiles $\{\hat{z}_m(x;\hat{z}_{m0})\}$ are zero. Figure 5 shows the above-mentioned procedure of the method proposed in this study for the accurate estimation of the surface roughness of the carotid arterial wall.

3. Basic Experiments Using Silicone Phantom

3.1 Determination of the optimal size of a correlation kernel

The estimated displacements $\hat{l}(m,n)$ and $\hat{d}_{\text{sp}}(m,n)$ depend on the size of the correlation kernel. Therefore, determination
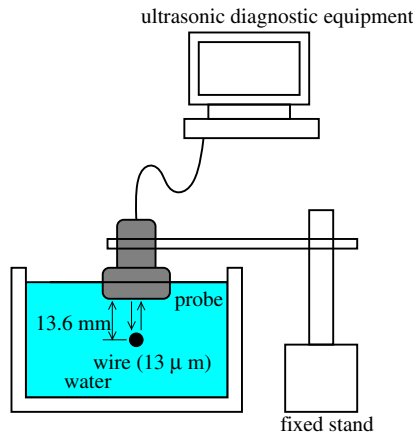
Fig. 6. (Color online) Illustration of system to measure ultrasonic beam profile.

Fig. 7. (Color online) Measured ultrasonic beam profile. (a) B-mode image of a fine wire (13 μm in diameter). (b) Profile in the axial direction. (c) Profile in the lateral direction.

of the optimal correlation kernel size is important. When the size of the correlation kernel is set to be small, there may be several regions in the post frame, which have echo patterns similar to those in the correlation kernel in the previous frame. These multiple regions, which have similar echo patterns, introduce misestimation of displacement. On the other hand, when the size of the kernel is set to be large, the echo pattern in the correlation kernel is more unique and the displacement estimation is less susceptible to noise. However, the profile around a peak of a normalized correlation function $C[\Delta l(m, n), \Delta d_{sp}(m, n)]$ becomes wider because it is rare that the echo patterns in two frames exactly coincide, which degrades the accuracy and the spatial resolution of the displacement estimation. In this study, the ultrasonic beam profile was measured to define the optimal kernel size as an integral multiple of the focal size. We used a 10 MHz linear-type probe of ultrasonic equipment (Aloka SSD-6500), with a sampling frequency of 40 MHz, a frame rate of 160 Hz, lateral beam intervals of 100 μm, and a pulse repetition frequency of 13 kHz. Figure 6 shows the system used to measure the ultrasonic beam profile. Figure 7(a) shows a B-mode image of a wire, which is 13 μm in diameter and is considered as a point scatterer (wavelength of ultrasound: 150 μm). The lateral and axial amplitude distributions along the red and green lines are shown in Figs. 7(b) and 7(c), respectively. The lateral and axial half-value widths, which were measured from Figs. 7(b) and 7(c), are 0.5 mm (lateral) and 0.2 mm (axial), respectively. Therefore, the lateral and axial widths of the kernel are defined as multiples of $\Delta w_l = 0.5$ mm and $\Delta w_d = 0.2$ mm, respectively, as follows:

$$W_l = 2\alpha \cdot \Delta w_l \text{ (mm)} \ (= 2\alpha \times 5 + 1 \text{ points}), \quad (15)$$

$$W_d = 2\alpha \cdot \Delta w_d \text{ (mm)} \ (= 2\alpha \times 10 + 1 \text{ points}), \quad (16)$$

where W_l and W_d are the lateral and axial kernel sizes, respectively, $\Delta w_l = 5$ points (0.5 mm), and $\Delta w_d = 10$ points (0.2 mm). In this experiment, the phantom, which includes point scatterers, and the ultrasonic probe were placed using an automatic stage and a static stand, respectively, as shown in Fig. 8. RF echos were acquired for 1.4 s during the movement of the phantom of ± 1.0 and ± 0.5 mm in the lateral and axial directions, respectively (lateral and axial velocities: 1.4 and 0.7 mm/s). The obtained B-mode image is shown in Fig. 9. In this study, the sizes W_l
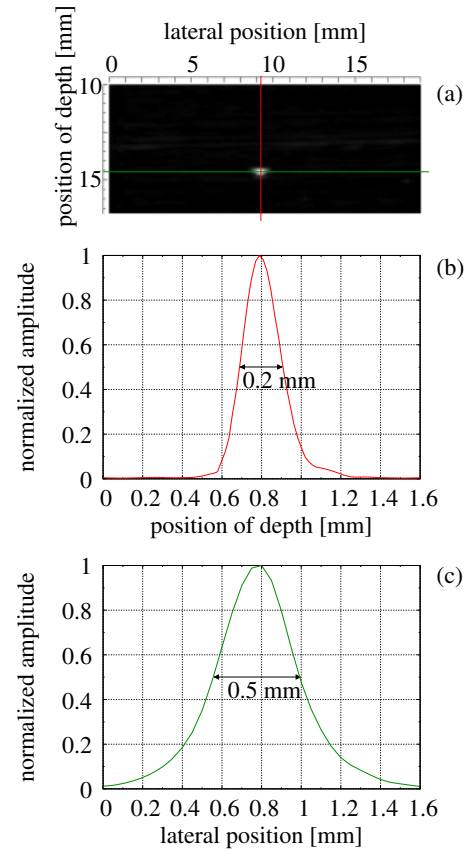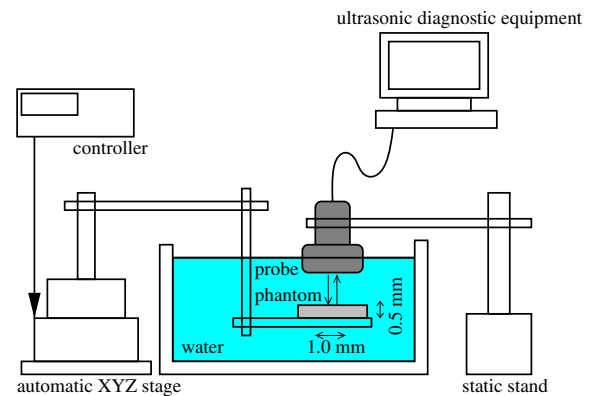

Fig. 8. (Color online) Illustration of system for basic experiment using a phantom.
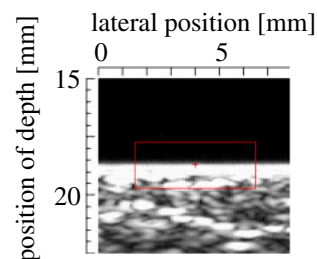

Fig. 9. (Color online) B-mode image of a phantom, which includes point scatterers. The red square is the optimal size (5.0×2.0) mm^2 of the correlation kernel and the red cross is the central position of the kernel.
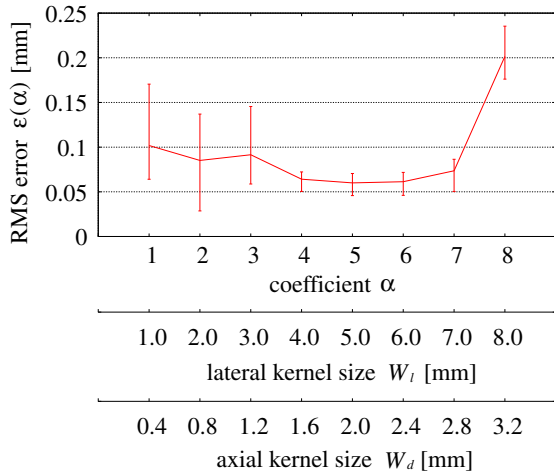
© 2012 The Japan Society of Applied Physics

Fig. 10. (Color online) Distribution of mean RMS errors {$\bar{\epsilon}(\alpha)$} for different sizes of kernels in seven measurements.

Fig. 11. (Color online) Distribution of mean RMS errors {$\bar{\epsilon}(\alpha_l = 5, \alpha_d)$} for different sizes of kernels in seven measurements.

and W_d of the correlation kernel in the lateral and axial directions, respectively, were defined by $\pm 2\alpha$. The optimal size ($W_l \times W_d$) of the correlation kernel was determined using the value of α when the RMS error of the estimated displacement from the actual displacement was smallest.

To calculate the RMS error $\epsilon(\alpha)$, the lateral and axial displacements were estimated using different values of α. The RMS error $\epsilon(\alpha)$ in the estimated lateral and axial displacements, which was evaluated for each value of α, was calculated from the estimated lateral displacement $l(m, n)$, the estimated axial displacement $d_{sp}(m, n)$, the actual lateral displacement $l_{ac}(m, n)$, and the actual axial displacement $d_{ac}(m, n)$ as follows:

$$\epsilon(\alpha) = \sqrt{\frac{1}{2N} \sum_{n=0}^{N-1} [\{l(m, n) - l_{ac}(m, n)\}^2 + \{d_{sp}(m, n) - d_{ac}(m, n)\}^2]}, \quad (17)$$

where N is the number of frames. The central position of the kernel was initially placed at the surface of the phantom. RMS errors {$\epsilon(\alpha)$} were calculated for seven measurements. The mean RMS errors {$\bar{\epsilon}(\alpha)$} are plotted in Fig. 10. In Fig. 10, error bars show the maximum and minimum values of the calculated RMS errors {$\epsilon(\alpha)$} for seven measurements. The mean RMS error $\bar{\epsilon}(\alpha)$ was smallest (0.055 mm) when the coefficient α was 5. Therefore, the optimal kernel size ($W_l \times W_d$) was determined as (5.0×2.0) mm^2. The determined optimal size is shown by the red square in Fig. 9. The axial length of the kernel is much smaller than the lateral length when the kernel size is determined by a single value of α, owing to uneven lateral and axial sizes of the ultrasonic point spread function. Therefore, separately defined magnification factors α_l and α_d are also investigated to examine smaller and larger axial lengths of the kernel. In Fig. 11, the mean RMS errors {$\epsilon(\alpha_l = 5, \alpha_d)$} are plotted as a function of α_d and α_l of 5. This result shows that α_d of 5 and α_l of 5 are optimal to estimate the lateral displacement of the arterial wall. This is because echoes from the inside of the arterial wall (i.e., tissues in the region deeper than the posterior wall) need to be included in the kernel because echoes from the luminal interface are similar among ultrasonic beams and there is no distinct echo pattern to be tracked. For comparison, lateral and axial displacements estimated at kernel sizes of {(0.8×0.8) mm^2},[32] {(2.0×1.5) mm^2},[33] and {(3.2×2.5) mm^2}[28] are shown in Figs. 12(a) and 12(c). Figure 12(b) shows lateral displacements estimated at kernel sizes of $\alpha = 5, 6, 7$, and 8. These results show that more accurate estimation of displacements of the phantom is possible using the optimal kernel ($\alpha = 5$) size than with
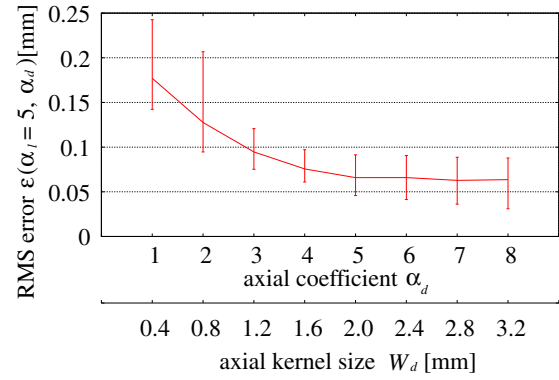
other kernel sizes. Also, the lateral displacements were estimated at three different depths of central position of the correlation kernel and were also estimated when the surface of the phantom is not parallel to the surface of the ultrasonic probe. Figures 13(a)–13(e) show B-mode images of the silicone phantom at a depth of 18.5 mm, a deeper depth of 25 mm, and a shallower depth of 12 mm, a B-mode image obtained when the surface of the phantom is not parallel to the surface of the ultrasonic probe, and the estimated lateral displacements, respectively. The RMS errors between the estimated lateral displacements and the actual values were 0.067 mm (18.5 mm), 0.071 mm (25 mm), 0.068 mm (12 mm), and 0.072 mm (leaning). These results show that the determined optimal kernel size can be applied for various depths and the case when the surface of the phantom is not parallel to the surface of an ultrasonic probe.

3.2 Estimation of surface roughness of the silicone phantom
In a basic experiment, we used a silicone phantom, which had ten saw tooth shapes on its surface. The phantom was moved in the lateral (back and forth by 1 mm) and axial (up and down by 0.5 mm) directions using an automatic stage to simulate arterial wall motion. To simulate the medium between the skin and the arterial wall, a piece of pork cutlet was put between the ultrasonic probe and the phantom. The system of this experiment was similar to the previous system shown in Fig. 8, except for the phantom and the pork cutlet. The obtained B-mode images of the phantom are shown in Figs. 14(a) and 14(b). Measurements were carried out three times. The estimated surface profiles $\hat{z}(x)$ from three
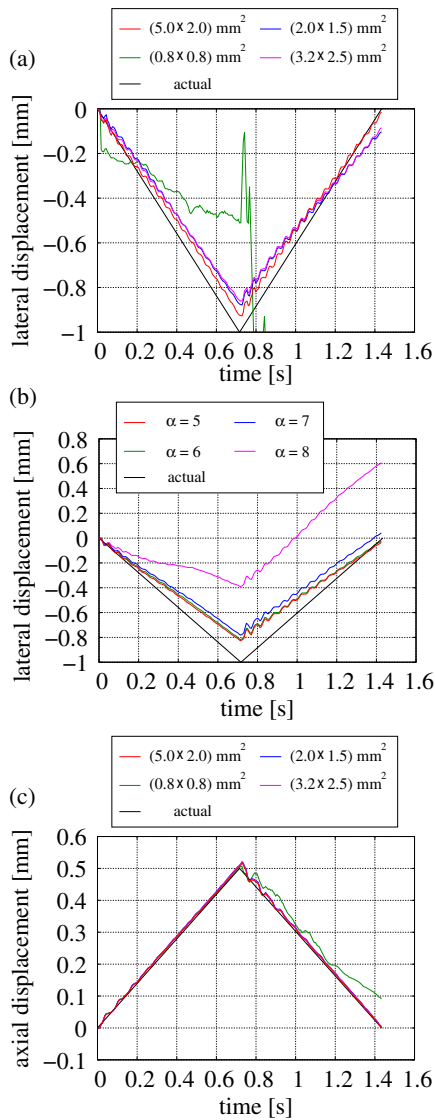
© 2012 The Japan Society of Applied Physics

Fig. 12. (Color online) (a) Estimated lateral displacements $\{l(m,n)\}$ and actual displacement $l_a(m,n)$ (black line). For comparison, displacements estimated using various kernel sizes, $(W_l \times W_d)$ of (5.0×2.0) mm^2 ($\alpha = 5$, red line), $\{(0.8 \times 0.8)$ mm$^2\}$[32] (green line), $\{(2.0 \times 1.5)$ mm$^2\}$[33] (blue line), and $\{(3.2 \times 2.5)$ mm$^2\}$[28] (pink line), are also shown. (b) Estimated lateral displacements $\{l(m,n)\}$ and actual displacement $l_a(m,n)$ (black line). For comparison, displacements estimated using various kernel sizes, $\alpha = 5$ (red line), $\alpha = 6$ (green line), $\alpha = 7$ (blue line), and $\alpha = 8$ (pink line), are also shown. (c) Estimated axial displacements $\{d_{sp}(m,n)\}$ and actual displacement $d_{spa}(m,n)$, (black line) which are shown in the same way as (a).

Fig. 13. (Color online) (a) B-mode image of the silicone phantom at a depth of 18.5 mm. (b) B-mode image of the silicone phantom at a deeper depth (25 mm). (c) B-mode image of the silicone phantom at a shallower depth (12 mm). (d) B-mode image of the silicone phantom when the surface of the ultrasonic probe and the silicone phantom are not parallel. (e) Estimated lateral displacements $\{l(m,n)\}$ and actual displacement $l_a(m,n)$ (black line). For comparison, displacements estimated at various depths and angles of the ultrasonic probe are also shown.

measurements and that measured using the laser profilometer are shown in Figs. 15(a) and 15(b). These results show that reproducible estimation of surface profiles $\hat{z}(x)$ for three measurements was possible. Also, the estimated periodicity pitches of saw tooth shapes agreed well with those obtained using the laser profilometer. These results show that the surface roughnesses of phantoms could be estimated by the proposed method. Moreover, in Figs. 15(a) and 15(b), red arrows show the magnitude of the lateral displacement of the phantom (1 mm). The results shown in Figs. 15(a) and 15(b) show that the regions of estimation of the surface profiles $\hat{z}(x)$ could be expanded by more than the magnitude of the lateral displacement of the object. The black solid line in Fig. 15(c) is the same as the result of the first measurement
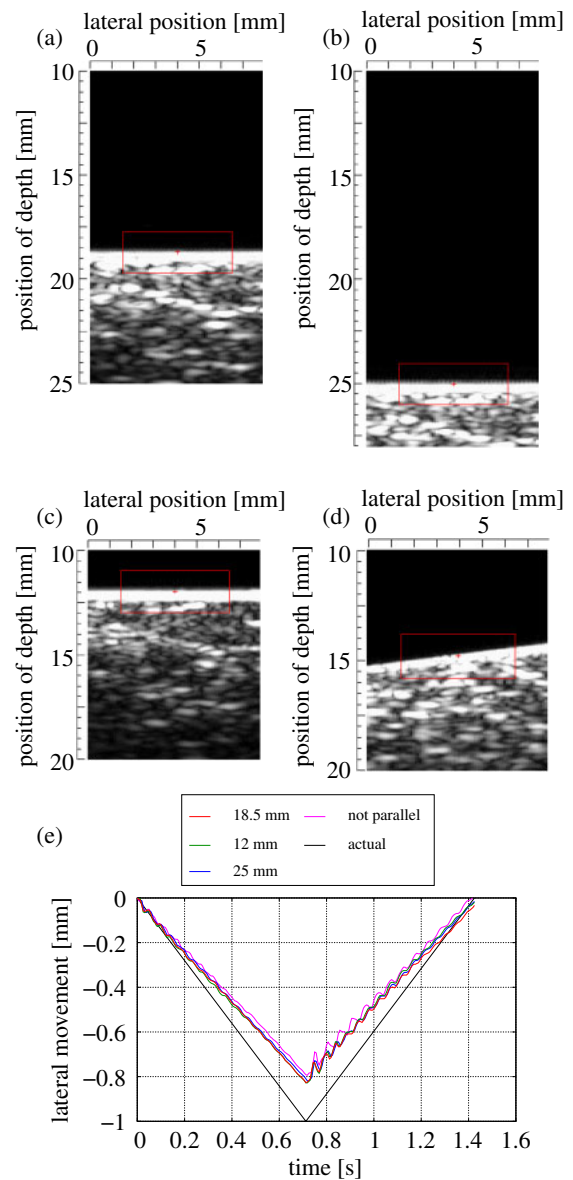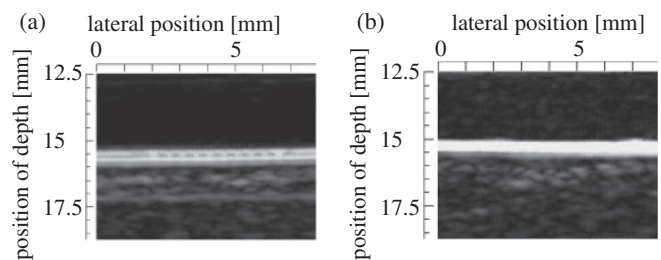

Fig. 14. B-mode images of a phantom which has ten saw tooth shapes on its surface. (a) Measurement with only water between ultrasonic probe and phantom. (b) Measurement with pork cutlet between ultrasonic probe and phantom.
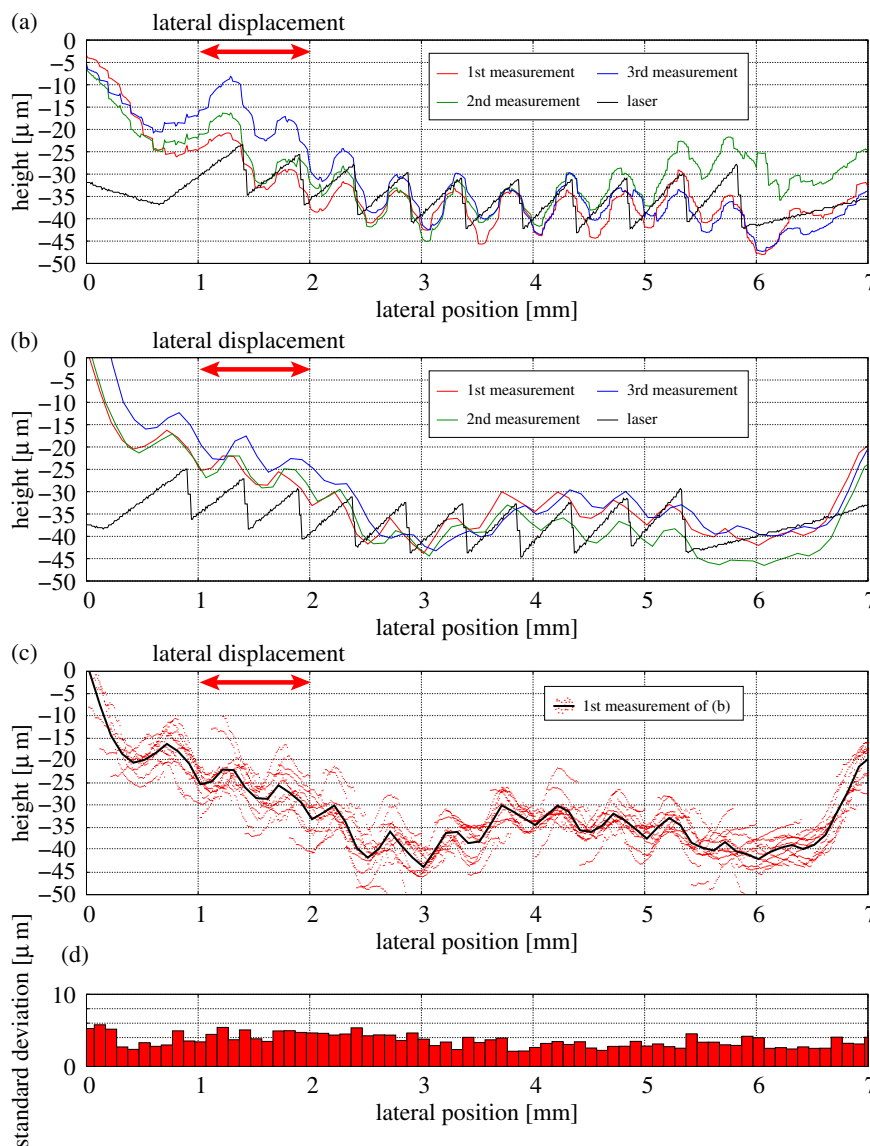
Fig. 15. (Color online) Estimated surface profiles $\{z(x)\}$ of the phantom for three measurements (red, green, and blue lines) and surface profile measured by the laser profilometer (black line). The red arrow shows the magnitude of lateral displacement of the phantom. (a) Measurement with only water between ultrasonic probe and phantom. (b) Measurement with pork cutlet between ultrasonic probe and phantom. (c) Estimated surface profile with pork cutlet between ultrasonic probe and phantom, which is the surface profile in (b) (red line). Red dots are surface profiles $\{\hat{z}_m(x; \hat{z}_{m0})\}$ estimated with respect to ultrasonic beams used for estimation. (d) Standard deviation of measured surface profiles in (c).

in Fig. 15(b). Red dots and the black solid line show the surface profiles $\{\hat{z}_m(x; \hat{z}_{m0})\}$ estimated with respect to the ultrasonic beams used for estimation and the averaged value, which corresponds to the surface profile $z(x)$, respectively. Moreover, Fig. 15(d) shows the standard deviation of the red dots in the z-direction. This result shows that a surface profile with a height smaller than $10\,\mu\text{m}$ could be measured using the proposed method.

3.3 Discussion of estimation of surface roughness on the silicone phantoms

The measured surface profiles $\{\hat{z}(x)\}$ depend on the assigned initial axial position z_{m0}. Figure 16 shows an RF signal from the surface of the phantom. The initial tracking position z_{m0} was manually assigned at $\beta = 6$ points (0.116 mm), 9 points (0.173 mm), 12 points (0.231 mm), 15 points (0.289 mm), 18 points (0.347 mm), and 21 points (0.404 mm) shallower than the point at the maximum value of the RF signal. The
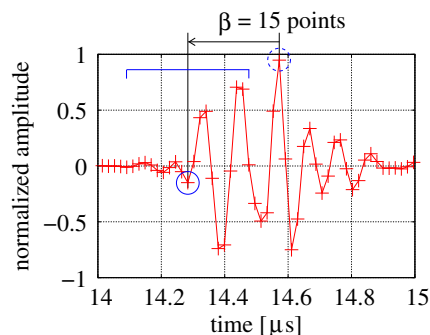

Fig. 16. (Color online) Acquired RF signal from the surface of the phantom. The blue bracket shows the width of the correlation kernel in phase tracking.

estimated surface roughnesses are shown in Figs. 17(a)–17(c). When the distance β is too large (e.g., 18 points and 21 points), the estimated surface roughness is significantly
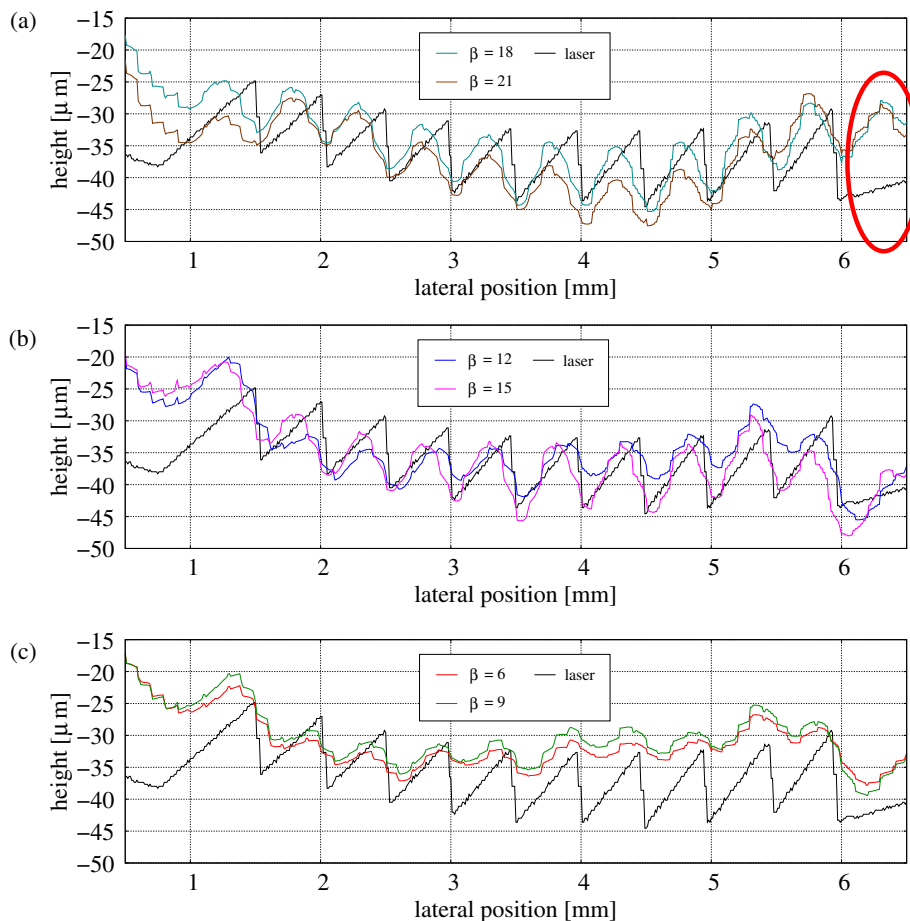
Fig. 17. (Color online) Estimated surface profiles of the phantom at various values of β (corresponding to the distance from the point at the maximum amplitude of the echo). (a) $\beta = 21$ points (brown line) and $\beta = 18$ points (cyan line). (b) $\beta = 15$ points (pink line) and $\beta = 12$ points (blue line). (c) $\beta = 9$ points (green line) and $\beta = 6$ points (red line).

degraded [as shown in the red ellipse in Fig. 17(a)]. This is because there is no effective RF echo from the surface of the phantom in the correlation kernel owing to the use of a Hanning window. On the other hand, when the distance β is too small (e.g., 6 points and 9 points), the estimated surface roughness is smaller than that measured by the laser profilometer. This is because the RF signal during 14.4–14.5 μs in Fig. 18(a) varies significantly owing to interference between RF signals from the top and bottom of the saw tooth shapes at their turning point. Figure 18(a) shows RF signals from various lateral positions of the saw tooth shape (i.e., the turning point of the saw tooth shape and other points). The fourth positive peak (during 14.4–14.5 μs) of these RF signals varied significantly compared with the others. Figure 18(b) shows RF signals from various lateral positions of another saw tooth shape, whose height is double that of Fig. 18(a). Figure 18(c) shows an RF signal (pulse signal) from a point scatterer. The RF signals in Figs. 18(a) and 18(b) were composed by two overlapping pulse signals, which were reflected from the top and bottom of the saw tooth shape because the full width at half maximum of the ultrasonic beam profile is 500 μm in the lateral direction. The variance of the amplitude of the fourth positive peak of these RF signals in Fig. 18(b) is larger than that in Fig. 18(a). This is because the height of the saw tooth in Fig. 18(b) is larger than that in Fig. 18(a). To analyze only the echo from the peak of the saw tooth shape, the optimal

initial axial position z_{m0} in phase tracking and block matching should be determined to be as shallower as possible. Therefore, the optimal initial axial position z_{m0} in phase tracking and block matching is determined to be $\beta = 15$ points because β larger than 18 points is not optimal, as described previously.

As shown in Figs. 15(a) and 15(b), both sides of the estimated surface profiles $\{z(x)\}$ deviated from the estimated surface profile measured by the laser profilometer. This is because the surface profile estimated by the proposed method corresponds to the convolution of the surface profile measured by the laser profilometer (actual surface profile) and the point spread function of ultrasound in the lateral direction. Figure 19 shows the surface profile obtained by convolution of the Gaussian function, which was assumed as the point spread function of ultrasound, to the surface profile measured by the laser pofilometer. As shown in Fig. 19, the convolved result deviated from the actual surface profile measured by the laser profilometer, as in Figs. 15(a) and 15(b). Therefore, both sides of the estimated surface profiles $\{z(x)\}$ deviated from the estimated surface profile by the laser profilometer because of the point spread function of ultrasound in the lateral direction. Also, the estimated saw tooth shapes became blurred.

The proposed method can be applied to the measurement of minute surface roughness in the case when the surface of the ultrasonic probe and the carotid arterial wall are not
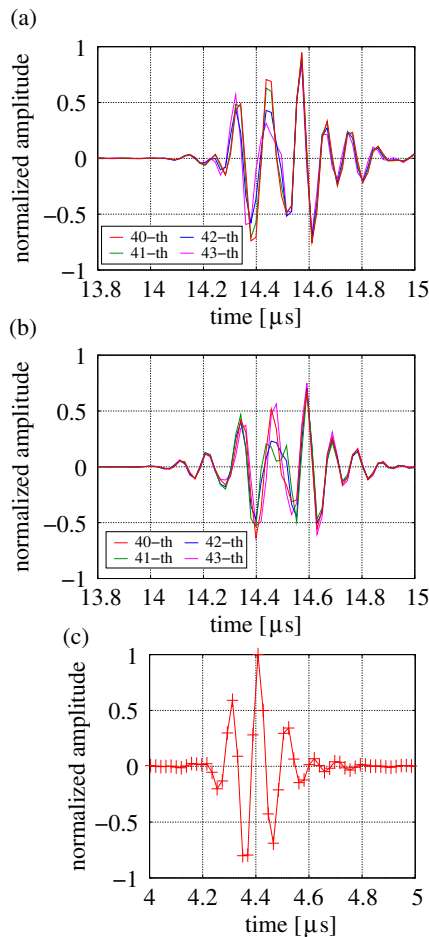
© 2012 The Japan Society of Applied Physics

Fig. 18. (Color online) (a) Acquired RF signal from surface of phantom (11 µm height) at each beam position. (b) Acquired RF signal from surface of phantom (22 µm height) at each beam position. (c) Acquired RF signal from a point scatterer.
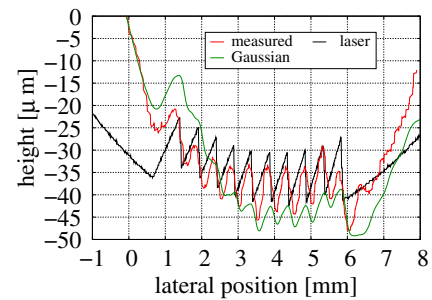

Fig. 19. (Color online) Estimated surface profile $z(x)$ by the proposed method (red line), and the result (green line) obtained by convolving the Gaussian function to the surface profile measured using a laser profilometer (black line).
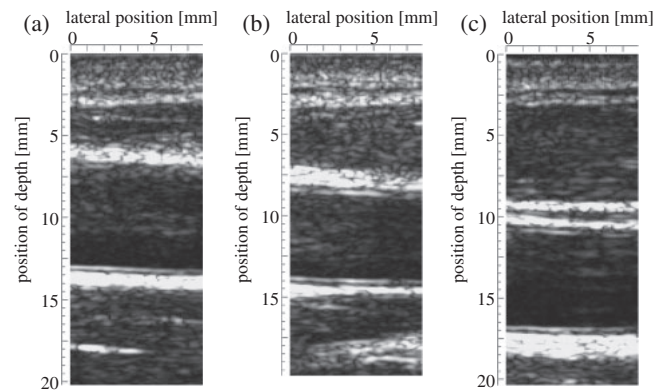

Fig. 20. B-mode images of carotid arteries obtained from subject A (24-year-old healthy male), subject B (23-year-old healthy male), and subject C (23-year-old healthy male). The direction of blood flow corresponds the direction from right to left. (a) Subject A. (b) Subject B. (c) Subject C.

parallel. This is because the axial displacement $d(m, n, \phi)$ estimated by the phased-tracking method is expressed by $d(m, n, \phi) = d(m, n) \cdot \cos \phi$, where ϕ is the angle between the probe and the arterial luminal surfaces. Also, the lateral displacement $l(m, n, \phi)$ estimated using block matching is expressed as $l(m, n, \phi) = l(m, n) \cdot \cos \phi$. The effect of the angle can be ignored because $\cos \phi$ is 0.9848 at a typical leaning angle of 10°. Moreover, as shown in Fig. 13(c), the optimal size of the correlation kernel $(W_l \times W_d) = (5.0 \times 2.0)\,\mathrm{mm}^2$ could also be applied for such a case.

4. *In vivo* Experimental Results

4.1 Acquisition of RF signals *in vivo*

The RF data of three subjects [subject A (24-year-old healthy male), subject B (23-year-old healthy male), and subject C (23-year-old healthy male)] were acquired during two heart beats. Figures 20(a)–20(c) show B-mode images of the arterial walls obtained from the three healthy males. The frame rates were set at 160 Hz. In this study, the RF data were acquired using a 10 MHz linear-type probe of ultrasonic equipment, which was the same as that used in the basic experiment. The optimal size of a correlation kernel $(W_l \times W_d) = (5.0 \times 2.0)\,\mathrm{mm}^2$ determined by the basic experiment was also used in the *in vivo* experiment. Also, the initial axial position z_{m0} is determined using the

distance β from the point at the maximum amplitude of the RF echo from the lumen-intima boundary.

4.2 Results of estimation of surface roughness *in vivo*

The lateral displacements $\{\hat{l}(m, n)\}$ of the arterial walls of the three subjects were measured during two heart beats. Figures 21(a)–21(c) show estimated lateral displacements $\{\hat{l}(m, n)\}$ during one cardiac cycle obtained from subject A, subject B, and subject C (negative lateral displacement corresponds to movement in the direction of blood flow), respectively. These results of estimated lateral displacements $\{\hat{l}(m, n)\}$ of the arterial wall were obtained using block matching and are reproducible. In addition, the estimated minute surface profiles $\hat{z}(x)$ of the carotid arterial wall of subject A, subject B, and subject C show the expanded region of estimation using the proposed method, as shown in Figs. 22(a)–22(c).

4.3 Discussion of estimation of surface roughness *in vivo*

The lateral displacements $\{l(m, n)\}$ of the arterial wall in the direction against the blood flow existed between the S wave and the T wave of the electrocardiogram and after the T wave of the electrocardiogram. In addition, the estimated surface profiles $\{\hat{z}(x)\}$ were similar between two beats. These results show that reproducible estimations of surface profiles $\{z(x)\}$ are possible using the proposed method. Moreover, in Figs. 22(a)–22(c), the red arrows show the magnitude of the
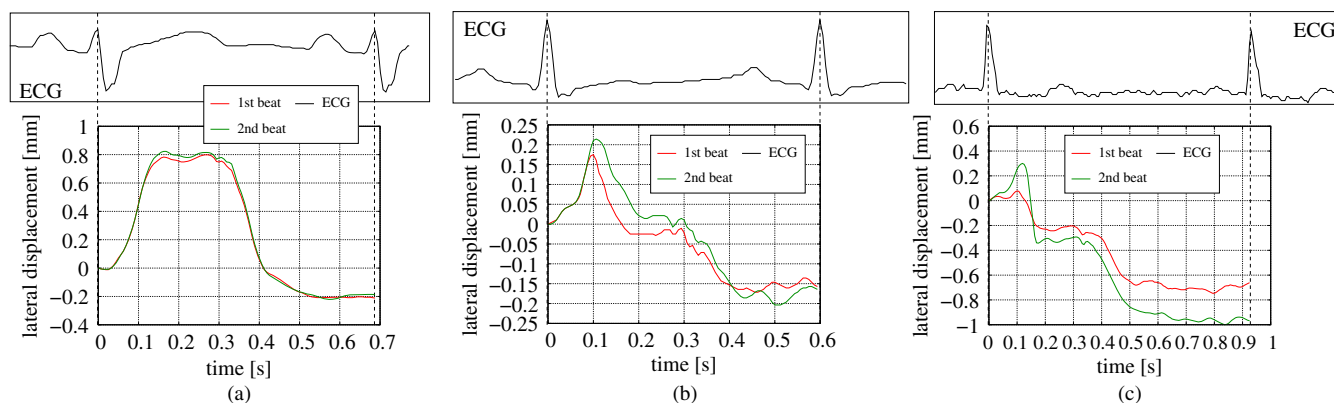
© 2012 The Japan Society of Applied Physics

Fig. 21. (Color online) Estimated lateral displacements of carotid arterial walls during one cardiac cycle (red and green lines) and electrocardiograms (ECGs) (black line) obtained from subject A (24-year-old healthy male), subject B (23-year-old healthy male), and subject C (23-year-old healthy male). Negative longitudinal displacement corresponds to movement in the direction of blood flow. (a) Subject A. (b) Subject B. (c) Subject C.
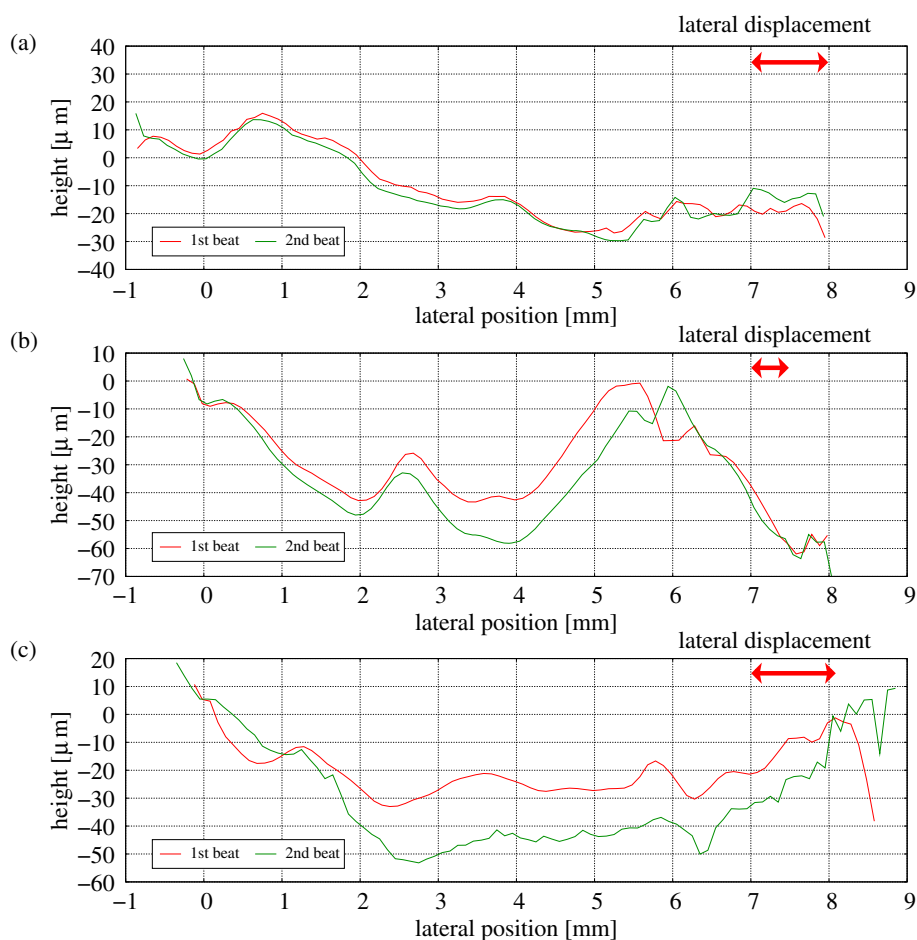

Fig. 22. (Color online) Estimated surface profiles of the carotid arterial wall obtained from subject A (24-year-old healthy male), subject B (23-year-old healthy male), and subject C (23-year-old healthy male). Red arrows show the magnitude of lateral displacement of arterial wall. (a) Subject A. (b) Subject B. (c) Subject C.

lateral displacements of arterial walls. These results show that regions of estimations of surface profiles $\{z(x)\}$ could be expanded by more than the magnitude of lateral displacement of the arterial wall.

For estimation of the lateral displacement, in the present study, the block matching technique based on correlation between RF echoes was used, and the correlation kernel size was optimized using a silicone phantom without any deformation. However, under the *in vivo* condition, there should be deformations of the arterial wall and external tissue, such as shearing due to blood flow and longitudinal motion of the artery. The lateral displacement estimated using a correlation window including echoes from media, adventitia, and external tissue in addition to that from the luminal interface would be influenced by the differences among displacements of intima, media, adventitia, and

© 2012 The Japan Society of Applied Physics

external tissue. Therefore, in a future work, it is necessary to further examine the optimum correlation kernel size using a phantom with deformation.

During one cardiac cycle, the anterior wall also moves laterally, and the luminal surface of the anterior wall may be rough. However, the effect of the surface roughness of the anterior wall on the estimation of the minute surface profile of the posterior wall is small. This is because the ultrasound only transmits though the anterior wall. If there is a surface roughness of $10\,\mu\text{m}$ on the anterior wall, the effect of the surface roughness of the anterior wall owing to lateral motion on the estimation results of the surface profile of the posterior wall is $0.19\,\mu\text{m}$ ($= 1570\,\text{mm}/1540\,\text{m/s} \times 10\,\mu\text{m} - 10\,\mu\text{m}$), because sound speeds in the arterial wall and in blood are 1540 and $1570\,\text{m/s}$, respectively.[27] Therefore, the effect of surface roughness of the anterior wall is negligible because it is smaller than the surface roughness of $10\,\mu\text{m}$ on the posterior wall, which is desired to be measured.

5. Conclusions

In this paper, we proposed a method for the accurate estimation of the surface roughness $z(x)$ of the carotid arterial wall. To expand the measured region, surface profiles $\{\hat{z}_m(x; \hat{z}_{m0})\}$ estimated at several ultrasonic beams were combined. In the basic experiment, the optimal kernel size for block matching was determined as $(W_1 \times W_d) = (5.0 \times 2.0)\,\text{mm}^2$. Then, the surface roughness of the carotid arterial wall (for three healthy subjects) could be estimated *in vivo* using the proposed method. The results of *in vivo* measurements show that the proposed method is applicable to the accurate estimation of the carotid luminal surface roughness. Further investigation will be conducted to measure the luminal surface roughness of the diseased carotid artery.

1) I. Wendelhag, O. Wiklund, and J. Wikstrand: Arterioscler. Thromb. Vasc. Biol. **16** (1996) 843.
2) Q. Liang, I. Wendelhag, J. Wilstrand, and T. Gustavsson: IEEE Trans. Med. Imaging **19** (2000) 127.
3) J. D. Klingensmith, R. Shekhar, and D. G. Vince: IEEE Trans. Med. Imaging **19** (2000) 996.
4) J. M. Meinders, P. J. Brands, J. M. Willigers, L. Kornet, and A. P. G. Hoeks: Ultrasound Med. Biol. **27** (2001) 785.
5) H. Kanai, H. Hasegawa, M. Ichiki, F. Tezuka, and Y. Koiwa: Circulation **107** (2003) 3018.
6) J. Maurice, J. Ohayon, Y. Frétigny, M. Bertrand, G. Soulez, and G. Cloutier: IEEE Trans. Med. Imaging **23** (2004) 164.
7) K. Tsuzuki, H. Hasegawa, and H. Kanai: Jpn. J. Appl. Phys. **47** (2008) 4180.
8) K. Ikeshita, H. Hasegawa, and H. Kanai: Jpn. J. Appl. Phys. **48** (2009) 07GJ10.
9) K. Ikeshita, H. Hasegawa, and H. Kanai: Jpn. J. Appl. Phys. **50** (2011) 07HF08.
10) R. Ross: N. Engl. J. Med. **340** (1999) 115.
11) E. Sho, M. Sho, T. M. Singh, H. Nanjo, M. Komatsu, C. Xu, H. Masuda, and C. K. Zarins: Exp. Mol. Pathol. **73** (2002) 142.
12) Y. Uehara, I. Saito, T. Kushiro, and F. Nakamura: *Hitomede-Wakaru Kekkan Syogai* (Vascular Disorders at a Glance) (MEDSi, Tokyo, 1995) [in Japanese].
13) B. J. Dean and P. C. Pedersen: Proc. IEEE Ultrasonics Symp., 1996, p. 693.
14) J. E. Wilhjelm, P. C. Pedersen, S. M. Jacobsen, and K. Martinsen: Proc. IEEE Ultrasonics Symp., 1998, p. 1839.
15) J. E. Wilhjelm, P. C. Pedersen, and S. M. Jacobsen: IEEE Trans. Ultrason. Ferroelectr. Freq. Control **48** (2001) 511.
16) K. Kudo, H. Hasegawa, and H. Kanai: Jpn. J. Appl. Phys. **46** (2007) 4873.
17) C. Arihara, H. Hasegawa, and H. Kanai: Jpn. J. Appl. Phys. **45** (2006) 4727.
18) M. Cinthio, Å. R. Ahlgren, T. Jansson, A. Eriksson, H. W. Persson, and K. Lindström: IEEE Trans. Ultrason. Ferroelectr. Freq. Control **52** (2005) 1300.
19) M. Cinthio, H. Hasegawa, and H. Kanai: IEEE Trans. Ultrason. Ferroelectr. Freq. Control **58** (2011) 853.
20) M. Cinthio, H. Hasegawa, and H. Kanai: Proc. IEEE Ultrasonics Symp., 2007, p. 997.
21) H. Kanai, Y. Kiowa, and J. Zhang: IEEE Trans. Ultrason. Ferroelectr. Freq. Control **46** (1999) 1229.
22) H. Kanai, M. Sato, Y. Kiowa, and N. Chubachi: IEEE Trans. Ultrason. Ferroelectr. Freq. Control **43** (1996) 791.
23) H. Kanai, K. Sugimura, Y. Kiowa, and Y. Tsukahara: Electron. Lett. **35** (1999) 949.
24) H. Yoshiara, H. Hasegawa, and Y. Kanai: Jpn. J. Appl. Phys. **46** (2007) 4889.
25) Y. Kanai and M. Tanaka: Jpn. J. Appl. Phys. **50** (2011) 07HA01.
26) H. Takahashi, H. Hasegawa, and Y. Kanai: Jpn. J. Appl. Phys. **50** (2011) 07HF16.
27) N. Koshi: *Choonpa no Kiso to Sochi* (Basis of Ultrasound Diagnostic System and Technology) (Vector·core, Tokyo, 1994) [in Japanese].
28) S. Golemati, A. Sassano, M. J. Lever, A. A. Bharath, A. Dhanjil, and A. N. Nicolaides: Ultrasound Med. Biol. **29** (2003) 387.
29) J. H. Velduis and G. W. Broudland: Image Vision Comput. **17** (1999) 905.
30) I. Cespedes, Y. Huang, J. Ophir, and S. Spratt: Ultrason. Imaging **17** (1995) 142.
31) Y. Honjo, H. Hasegawa, and H. Kanai: Jpn. J. Appl. Phys. **49** (2010) 07HF14.
32) L. N. Bohs, B. H. Friemel, B. A. McDermott, and G. E. Trahey: Ultrasound Med. Biol. **19** (1993) 751.
33) G. E. Trahey, J. W. Allison, and O. T. von Ramm: IEEE Trans. Biomed. Eng. **34** (1987) 965.